SCATTERED LIGHT CHARACTERISTICS OF THE HUBBLE SPACE TELESCOPE FAINT OBJECT SPECTROGRAPH (SV #1319)

F. Bartko, *Bartko Science & Technology*
G. Burks, *University of Colorado, CASA*
G. Kriss and A. Davidsen, *Johns Hopkins University*
R. Cohen, V. Junkkarinen, R. Lyons,
University of California, San Diego, CASS

Instrument Science Report CAL/FOS-073
April, 1992

Abstract

Observations of a standard star (BD+75D325) have been used to measure the Hubble Space Telescope (HST)/ Faint Object Spectrograph (FOS) scattering characteristics in the wavelength range 115 to 250 nm. Spectra of the standard star were obtained as the star was progressively offset from the optical line of sight axis of the telescope, both in the in-dispersion and cross-dispersion directions.

These data have been reduced and analyzed to determine the scattering function of the telescope-spectrograph combination. Two primary results have been obtained. (1) The resulting scattering function exhibits three characteristics: (a) The inner core ($\theta < 4''$) is dominated by the large PSF of the HST; (b) the outer wings of the scattering function ($4'' < \theta < 32''$) show a θ^{-3} dependence consistent with predictions for the HST Airy disc; and (c) The wavelength dependence of this scattering function follows approximately λ^{-1}, suggesting that the UV micro roughness contribution to the scatter is quite small, and hence the HST primary mirror is very smooth at ultraviolet wavelengths. (2) The FOS scattering contribution is limited only by grating scatter, and is consistent with pre-launch grating calibration measurements.

As a result, both the scatter contribution from the HST mirror surface micro roughness and the FOS gratings appear to be within their design specifications. We also describe the implications of these results for FOS on achieving its limiting performance for certain typical observations.

1.0 Introduction

Several techniques are available for the determination of scattered light levels in spectrographs such as the FOS. One may look at the cores of saturated absorption lines, and determine the corrections necessary to produce zero levels at the line centers. This procedure had been used to correct data for background in the spectra of QSOs obtained with FOS. However, the relatively low resolution of the FOS may not permit a definitive

measure of this background and its subsequent resolution into the contributing components.

A "red leak" scattered light test has been considered and analyzed by Blair *et al* (1989) and Uomoto *et al* (1989) and reported elsewhere. Also Caldwell (1991) compared the FOS UV response with the GHRS UV response to a bright solar type star, and observed out of order scatter due to the FOS gratings, at a level which is consistent with the results reported here.

A specific test was suggested by W. Fastie for the HST, and devised by A. Davidsen for the FOS. In this test, a bright star is measured on axis, and then incrementally offset in several steps. A spectrum of the star is recorded at each off axis position. The procedure is carried out along the in dispersion and cross dispersion directions. It is this test procedure which is described and analyzed here.

The Faint Object Spectrograph (FOS) on the Hubble Space Telescope (HST) has been used to measure the scattering characteristics arising from their combined optical paths. The measurement is part of the Science Verification observations (SV 1319) performed during the early phases of HST operations. We determined the scattering function by observing a standard star (BD+75D325, spectral type = 05p, V = 9.54, B-V = 0.32) at a series of predetermined offset positions, both in the in-dispersion and the orthogonal cross dispersion directions. The resulting spectra were partially processed with CALFOS at UCSD. This report describes the details of the observations that were made, the reduction procedures that were applied to the data, and the results and conclusions that were derived from the analysis of the reduced data.

2.0 Observations

The data in the science verification test were obtained on March 9th and 10th of 1991. All observations were obtained with the FOS Blue detector. Since the standard star BD+75D325 is too bright for a binary search acquisition with the camera mirror, a series of peak up acquisitions, described below, were used to center the star in the FOS apertures, with the FOS configured to the G130H grating.

In the first step of the target acquisition sequence using the 1.0 arc sec circular aperture (B3), a 6 × 6 peak up sequence performed dwell scans that moved the telescope in 0.7 arc sec increments over a 3.5 arc sec field. For Reference, Figure 1 shows the sizes and locations of the FOS apertures, and notes the relationship of the peak up increments to the FOS coordinate system for both detectors.

A second acquisition step incorporated a 5 × 5 peak up sequence using the 0.3 arc sec circular (B2) aperture. The dwell scan sequence used 0.2 arc sec increments over an 0.8 arc sec field.

The final sequence applied another 5 × 5 peak up with the 0.3 arc sec aperture, using

increments of 0.05 arc sec to center the star in the aperture. Approximately 2 hours were required to complete the target acquisition sequence.

The FOS was then configured to the G160L low resolution mode, (R $\approx$ 200) grating. The 1.0 arc sec aperture, and the ACCUM data mode (XSTEPS = 4, OVERSCAN = 5, INTS = 1, SLICES = 1; PATTERNS and livetime parameters were varied to provide the desired integration times). With the standard star centered in the aperture, a 1 sec exposure was obtained for the on-axis reference spectrum. The HST was then commanded to offset the standard star from the telescope optical axis in various angular increments, in the in-dispersion direction, according to the offsets indicated in Table 1. As the telescope offsets the standard star from the telescope line of sight optical axis, the integration times and apertures are adjusted to maintain an adequate level of counts for good signal to noise.

The same procedure was repeated for the cross-dispersion direction. The standard star was again acquired and centered in the aperture through a series of target acquisition peak ups, followed by the ACCUM data mode to obtain spectra of the standard star at the same set of offset positions.

The data log for this entire set of observations is shown in Table 2. The root name of the data files are identified for each set of measurements described. The Y0HW0101T - Y0HW0103T files are the target acquisition data. The Y0HW0104T - Y0HW010BT files are the spectra obtained for each desired off set position in the in-dispersion direction. The Y0HW020* series are the data files for the corresponding target acquisition and offset positions in the cross dispersion direction. Table 3 provides additional details of the observations, including the actual observation times/dates, the integration times, and observational mode used.

Table 1. Standard Star Observations

Aperture	Integration Time(sec)	Offset Angle(arc sec)
B-3 1.0″	5	1.0
B-3 1.0″	20	2.0
B-3 1.0″	100	4.0
A-1 4.3″	10	4.0
A-1 4.3″	60	8.0
A-1 4.3″	480	16.0
A-1 4.3″	960	32.0

Table 2. SV1319 Data Log

Faint Object Spectrograph (FOS) Observation Log

Root name	Date	DETEC	fgw	ap	YBASE	Target name
Y0HW0101T	09/03/91	BLUE	H13	B-3	-677	BD+75D325
Y0HW0102T	09/03/91	BLUE	H13	B-2	-677	BD+75D325
Y0HW0103T	09/03/91	BLUE	H13	B-2	-677	BD+75D325
Y0HW0104T	09/03/91	BLUE	L15	B-3	-920	BD+75D325
Y0HW0105T	09/03/91	BLUE	L15	B-3	-920	BD+75D325
Y0HW0106T	09/03/91	BLUE	L15	B-3	-920	BD+75D325
Y0HW0107T	09/03/91	BLUE	L15	B-3	-920	BD+75D325
Y0HW0108T	09/03/91	BLUE	L15	A-1	-920	BD+75D325
Y0HW0109T	09/03/91	BLUE	L15	A-1	-920	BD+75D325
Y0HW010AT	09/03/91	BLUE	L15	A-1	-920	BD+75D325
Y0HW010BT	09/03/91	BLUE	L15	A-1	-920	BD+75D325
Y0HW0201T	09/03/91	BLUE	L15	B-3	-677	BD+75D325
Y0HW0202T	09/03/91	BLUE	H13	B-2	-677	BD+75D325
Y0HW0203T	09/03/91	BLUE	H13	B-2	-677	BD+75D325
Y0HW0204T	09/03/91	BLUE	H13	B-3	-920	BD+75D325
Y0HW0205T	09/03/91	BLUE	L15	B-3	-920	BD+75D325
Y0HW0206T	09/03/91	BLUE	L15	B-3	-920	BD+75D325
Y0HW0207T	09/03/91	BLUE	L15	B-3	-920	BD+75D325
Y0HW0208T	09/03/91	BLUE	L15	A-1	-920	BD+75D325
Y0HW0209T	09/03/91	BLUE	L15	A-1	-920	BD+75D325
Y0HW020AT	10/03/91	BLUE	L15	A-1	-920	BD+75D325
Y0HW020BT	10/03/91	BLUE	L15	A-1	-920	BD+75D325

Table 3. SV1319 Data Log Description

Date/Time	Description		Data Type	θ''
91.068/ 07:54:51.0	FOS Observation:	Y0HW0101	Peakup	
	Aperture:	A1_0		
	Expo time:	0.100 sec		
91.068/ 09:14:46.0	FOS Observation:	Y0HW0102	Peakup	
	Aperture:	A0_3		
	Expo time:	0.100 sec		
91.068/ 09:36:49.0	FOS Observation:	Y0HW0103	Peakup	
	Aperture:	A0_3		
	Expo time:	1.000 sec		
91.068/ 09:59:54.0	FOS Observation:	Y0HW0104	ACCUM	zero
	Aperture:	A1_0		
	Expo time:	1.000 sec		
91.068/ 11:11:55.0	FOS Observation:	Y0HW0105	ACCUM	1.0
	Aperture:	A1_0		
	Expo time:	5.000 sec		
91.068/ 11:15:56.0	FOS Observation:	Y0HW0106	ACCUM	2.0
	Aperture:	A1_0		
	Expo time:	20.000 sec		
91.068/ 11:19:58.0	FOS Observation:	Y0HW0107	ACCUM	4.0
	Aperture:	A1_0		
	Expo time:	100.000 sec		
91.068/ 11:26:31.0	FOS Observation:	Y0HW0108	ACCUM	4.0
	Aperture:	A4_3		
	Expo time:	10.000 sec		
91.068/ 11:30:36.0	FOS Observation:	Y0HW0109	ACCUM	8.0
	Aperture:	A4_3		
	Expo time:	60.000 sec		
91.068/ 12:48:44.0	FOS Observation:	Y0HW010A	ACCUM	16.0
	Aperture:	A4_3		
	Expo time:	480.000 sec		
91.068/ 14:25:32.0	FOS Observation:	Y0HW010B	ACCUM	32.0
	Aperture:	A4_3		
	Expo time:	960.000 sec		
91.068/ 17:35:06.0	FOS Observation:	Y0HW0201	Peakup	
	Aperture:	A1_0		
	Expo time:	0.100 sec		
91.068/ 18:55:02.0	FOS Observation:	Y0HW0202	Peakup	
	Aperture:	A0_3		
	Expo time:	0.100 sec		
91.068/ 19:17:05.0	FOS Observation:	Y0HW0203	Peakup	
	Aperture:	A0_3		
	Expo time:	1.000 sec		
91.068/ 19:40:10.0	FOS Observation:	Y0HW0204	ACCUM	zero
	Aperture:	A1_0		
	Expo time:	1.000 sec		
91.068/ 20:52:42.0	FOS Observation:	Y0HW0205	ACCUM	1.0
	Aperture:	A1_0		
	Expo time:	5.000 sec		
91.068/ 20:56:43.0	FOS Observation:	Y0HW0206	ACCUM	2.0
	Aperture:	A1_0		
	Expo time:	20.000 sec		
91.068/ 21:00:45.0	FOS Observation:	Y0HW0207	ACCUM	4.0
	Aperture:	A1_0		
	Expo time:	100.000 sec		
91.068/ 21:07:18.0	FOS Observation:	Y0HW0208	ACCUM	4.0
	Aperture:	A4_3		
	Expo time:	10.000 sec		
91.068/ 21:11:23.0	FOS Observation:	Y0HW0209	ACCUM	8.0
	Aperture:	A4_3		
	Expo time:	60.000 sec		
91.068/ 22:29:30.0	FOS Observation:	Y0HW020A	ACCUM	16.0
	Aperture:	A4_3		
	Expo time:	480.000 sec		
91.068/ 00:06:16.0	FOS Observation:	Y0HW020B	ACCUM	32.0
	Aperture:	A4_3		
	Expo time:	960.000 sec		

3.0 Data Reduction and Analysis

All data were processed through selected portions of CALFOS at UCSD. Using FOS calibration data, CALFOS performs various operations on the raw GEIS data files, such as bad pixel removal, flat field corrections, dark count subtraction, wavelength calibration, and conversion of data files from counts versus pixels to fluxes versus wavelength, using inverse sensitivity calibration values.

We used the raw data files and corrected for dead diodes and overscanning. These files were then piped over the network from UCSD to U. Colorado for further reduction. The IRAF data reduction system was then used to further reduce and analyze the data.

Using IRAF routines such as *splot*, the spectra were displayed and subsequently reduced. The raw spectra that we obtained are collected into two sets which are shown in Figure 2 for the in-dispersion measurements, and in Figure 3 for the cross dispersion measurements.

For each set, the series of offset spectra were first normalized by their integration times to convert the data to count rates, and then subsequently normalized by effective aperture area. Once the data were normalized, we then took the spectrum for each of the offset positions, and divided them by the on-axis reference spectrum. The divided spectra then gave residual count rates at each off-set location.

The normalized count rates are illustrated in Figure 4 for the in-dispersion data, and in Figure 5 for the cross-dispersion data. A number of features should be noted here. First, there is a slight color dependence present in the normalized count rates, (especially for the larger offset positions $\theta > 4''$ i.e. the residual count rates, at 120 nm, are approximately twice the value at 240 nm. Second, the geocoronal Lyman alpha emission appears in both first and second order, when the change over to the large aperture (4.3 arc sec) occurs at the offset pointing location of 4.0 arc secs.

To analyze the data further, we selected 4 spectral wavelength bins in each of the residual spectra shown. These regions are: (1) 95-110 nm (which should contain no light since the detector faceplate window (MgF_2) transmission cuts off at 115 nm), (2) 125 to 140 nm, (3) 170-190 nm, and (4) 225-240 nm. We then ran the IRAF task *splot* to calculate the mean count rates in each of these wavelength bins at each offset location. These mean count rates were then collected and plotted using the IRAF task *graph*. The results are shown in Figures 6 and 7, and show the mean residual count rates at each offset location, as a function of the offset location. These curves represent the HST/FOS scattering function. The values used in these figures are listed in Appendix A.

Figure 6 shows the mean count rate for spectral intervals (2), (3), and (4) defined above, versus offset position. The jagged feature shown at the 4.0 arc sec offset location is due to the changeover from the 1.0 arc sec diameter aperture to the larger 4.3 arc sec square aperture.

A similar procedure was followed for the cross-dispersion data. Figure 7 shows the cross-dispersion data compared with the in-dispersion data for the wavelength bins 170-190 nm and 95-110 nm. Note the offset between spectral bin (1) and spectral bin (3). The ratio of the mean count rate in 170-190 nm to the mean count rate in 95-110 nm is approximately 1/350, a value entirely consistent with grating scatter (see Figure 9).

The scattering function derived is essentially azimuthally symmetric except in the inner core. This is due to the fact that the pixel dimensions are different in the in-dispersion (40 μm wide, corresponding to 0.25 arc sec) and the cross dispersion direction (140 μm high corresponding to 1.4 arc sec). Hence, as the star image is offset in either direction, the diodes will be illuminated differently.

4.0 Results and Discussion

Several properties of the scattering function derived in the previous section are noted here. First, the fall off in the scattering function in the inner core ($\theta < 4''$) is dominated by the HST point spread function (PSF), while the outer wings ($4'' < \theta < 32''$) are dominated by HST primary mirror scatter. According to Brown and Burrows, (1990) and Hasan (1992), the far wings of this function are composed of a combination of Airy disk (θ^{-3}) and surface microroughness ($\theta^{-2.19}$) contributions. We have fit the wings of the scattering function seen in Figure 8, and have determined an angular dependence of θ^{-3}, which is primarily consistent with the theoretical predictions for an Airy disc contribution. Hence, microroughness scatter appears to be extremely small, even at these ultraviolet wavelengths. (See below.)

Next, the scattering function for the spectral bin 95 - 110 nm, is shown in Figure 7 for both the in-dispersion and cross dispersion directions. This function shows nearly the same angular dependence to that seen in the scattering function for the illuminated portion of the FOS grating wavelength bins (2), (3), and (4) except for an offset in scale of 3×10^{-3}. Since the FOS digicon face plate consists of magnesium flouride, with a well-known transmission cut off at 115 nm, no photons should be counted in this spectral bin. However, we see that appreciable count rates are in fact observed, and furthermore, exhibit an angular dependence similar to that seen for wavelength bins (2), (3) and (4). If this count rate were due strictly to dark count, no such angular dependence would occur. We interpret this contribution as due to FOS grating scatter.

This conclusion may be verified by studying the scattering characteristics of the individual FOS grating components that were measured at Johns Hopkins University, several years before integration into the FOS instrument. A typical grating line spread function is shown in Figure 9. From this data, we can estimate the number of counts that might be expected in this spectral bin (1) when a star is illuminating the grating over its range of sensitivity. We find that the offset in count rates and their angular dependence shown in this spectral bin, are entirely consistent with grating scatter.

Finally, the wavelength dependence seen earlier in the normalized count rates illustrated in Figures 4 and 5 and reported for $\theta = 16''$ in Figure 10, show a higher count rate ($\sim$2 $\times$) at the shortest wavelengths relative to the longer wavelengths. The residual spectra follow roughly a λ^{-1} dependence. The origin of this dependence is believed to be due to the microroughness structure in the HST primary mirror. We have also considered the possible effect of the dark count on this apparent wavelength dependence. In the on axis spectrum, the dark count is negligible, while in the off axis spectrum (32″), the dark count is approximately 1/3 of the flux at 180 nm. In this case the dark count contributes approximately 1/2 of the counts at 125 nm and about 1/4 of the counts at 220 nm. As a result, the dark count should provide about a 30% difference. However, the observed difference is $\sim$250%. Thus, the vast majority of the wavelength dependence is due to "scattering" and not due to the effect of unsubtracted dark count.

In other investigations, Hasan (1992) has concluded that the UV microroughness scatter from the HST does not appear to be significant at visible wavelengths. The analysis by Hasan, using WF/PC data on a bright star HD95418 (V = 2.35), with 3 different filters (F889N, F487N, and F284W) indicate that very little or no contribution from microroughness scatter in the HST primary mirror is apparent at these wavelengths studied. Our results suggest that the microroughness scatter contribution is small even at these UV wavelengths, and indicate that the HST primary mirror surface is extremely smooth.

5.0 Implications for FOS Observations

a) Contamination from Nearby Objects

The scattering function shown in the previous discussions may have a significant impact on FOS observations of extended objects, objects in crowded fields, and measurements of faint structures such as QSO fuzz containing a bright nearby point source. In each of these observations, a portion of the light from the undesired nearby object, will contaminate the desired spectra to a degree which depends of the angular separation or offset of the bright unwanted source from the desired target source. Using the derived scattering function, we can estimate the degree of contamination due to scattered light.

For this illustration, we use the results for the wave band between 170-190 nm. Imagine two nearby stars, where the the target star has m = 16. A brighter star 2″ off axis, along the dispersion axis, would provide 10% of the light to the spectrum of the centered star if it had a magnitude of m = 13.5. If the brighter star were 4″ off axis it would need to have m = 8.25. In the direction perpendicular to the dispersion direction at 2″ off, m = 11.15 is needed; at 4″, m = 8.35. Thus, we can tolerate contamination from sources as near as 4″, and as bright as 8th magnitude.

Next, consider the case of diffuse fuzz near QSOs. Imagine that we want to study a diffuse knot with a radius of 1″ near a QSO with m = 16. If the spectrum is centered on the knot, what brightness density would that knot need to have to provide at least half of

the light in the FOS spectrum? A contamination of 50% is possibly the maximum that can be usefully deconvolved and hence tolerated. First in the in-dispersion direction; at 1″ from the QSO, the knot must have m = 18.4 per square arc sec; at 2″, m = 20.25; and at 4″, m = 25.5. For the case perpendicular to the dispersion axis, we see at 1″ from the QSO, the knot must have m = 18.5; at 2″, m = 21.6; and at 4″, m = 25.4. Thus, it would be possible to observe a faint (m=20-21) diffuse knot as close at 2″ from a bright QSO. Other combinations of single and multiple sources or extended sources may also be considered, but are too varied to be generalized.

b) Background Contamination

In a recent specific observation, the QSO PKS 0454-22 was observed with FOS over the spectral region 115-285 nm using the G130H, G190H, and G270H (R = 1300) gratings, in conjunction with the blue detector and the 1.0 arc sec circular aperture. The line centers of saturated UV lines were noted to exhibit non-zero light levels. Since these lines should be black at their centers, extraneous background contaminated the line centers. We attempted to estimate the level of this contribution, by considering several possible sources, e.g. grating scatter of continuum, geocoronal Ly Alpha and O I; and diffuse background starlight.

In the spectrum of PKS 0454-22, the measured flux at 133 nm was found to be 1.13e-15 ergs cm^{-2} s^{-1} A^{-1}. The flux should have been very close to zero because this wavelength region is lower than the Lyman cutoff for a strong absorption system. The wavelength resolution element at this wavelength is 0.10 nm. The effective HST/FOS efficiency is $\approx$ 0.005, the aperture throughput is 0.25, and the conversion coefficient is 2.28e12. The resulting expected count rate is 3.2×10^{-3} counts/(sec•diode). We found that the ratio of the flux in the 95 nm to 115 nm band to the flux in the 170 nm to 190 nm band in the standard star spectrum to be $\approx$ 1/350. This flux is due to grating scattering since no light of the shorter wavelengths enters the detector. Thus, grating scatter will fill in the bottom of saturated lines to a value of the order of 1/350 of the continuum of the spectrum as a whole, if the spectrum is approximately flat. The continuum in the 137.5 nm to 147.5 nm region of the PKS 0454 spectrum is approximately 5.4e-15 erg cm^{-2} s^{-1} A^{-1}. If this value is multiplied by 1/350, we arrive at an approximate contribution due to grating scatter. This contribution results in a mean count rate of $\approx$ 9.1e-6 counts/(sec•diode).

The contribution of geocoronal Lyman Alpha emission is estimated to be (1.05e-12)(1e-5)(2e-3)(0.25)(0.871)(1215)(2.28e12) = 1.3e-5 counts/(sec•diode), while, the OI contribution is estimated to be $\approx$ 9.0e-6 counts/(sec•diode).

The effective galactic light contribution is likewise estimated to be 5e-6 counts/(sec•diode). If we sum all contributions including a dark count of 2.8e-3, we obtained a value of 2.89e-3 counts/(sec•diode). This value compares favorably with the results shown previously in Figure 7, when the dark count is subtracted.

We have also considered other effects, such as the effect of scattered red light contamination due to out of order grating scatter. This can be an important effect when the UV spectrum of an object is $\sim 10^{-3}$ of the object visible/red light flux component. Our estimates for out of order grating scatter are consistent with the results obtained in the red scattered light analyses done by Blair *et al* (1989), Uomoto *et al* (1989) and Caldwell (1990).

Acknowledgements: We greatfully acknowledge useful discussions with George Hartig, Holland Ford, Richard Harms, Bill Fastie, and Bob Brown. This work was supported from NASA grant NASA NAS 5-29293.

6.0 References

Blair, W. P. *et al*, "Scattered Light Perpendicular to the Dispersion in the FOS", JHU CALFOS Report #058, Feb. 1989.

Brown, R. A. and Burrows, C. J., "On the Feasibility of Detecting Extra Solar Planest by Reflected Star Light using the Hubble Space Telescope", *ICARUS*, **87**, 484-497, 1990.

Burrows, C. J., "Hubble Space Telescope Optical Telescope Assembly Handbook", Version 1.0, STScI, May, 1990.

Caldwell, J. "FOS/GHRS Measurements of 16 Cyg B", Dec. 1991.

Ebbets, D., and Heap, S. R., "Science Verification Program for the Goddard High Resolution Spectrograph of the Hubble Space Telescope:, Final Report", Ball Aerospace, Feb 24, 1992.

Ford, H. C., "Faint Object Spectrograph Handbook", Space Telescope Science Institute, Oct. 1985.

Harms, R. J. *et al* "Astronomical Capabilities of the Faint Object Spectrograph on Space Telescope", IAU Commission 44, *The Space Telescope Observatory*, Aug. 1982.

Hasan, H., "Point Spread Function Scattering Test", Instrument Science Report - OTA, STScI, Feb. 27, 1992.

Stover, J. C., "Optical Scattering", McGraw Hill, 1990.

Uomoto, A. *et al* "Scattered Light Perpendicular to the Dispersion in the FOS", JHU, CALFOS Report #059, March 1989.

7.0 Figures

Figure Captions

Figure 1. An illustration of the FOS entrance apertures and locations, relative to HST and FOS coordinates.

Figure 2. Spectra of standard star obtained at various offset locations (θ) in the in dispersion direction. The plots show counts versus wavelength.

Figure 3. Spectra of standard star obtained at various offset locations (θ), in the cross dispersion direction. Again, the plots illustrate counts versus wavelength.

Figure 4. Residual spectra at each offset location for the in dispersion direction. These spectra result from dividing each offset spectrum by the on-axis reference spectrum of the standard star.

Figure 5. Residual spectra at each offset location for the cross dispersion direction, obtained as indicated for Figure 4. Note the slight wavelength dependence (λ^{-1}) for the residual spectra in Figures 4 and 5, for off set angles $\theta > 4''$.

Figure 6. Normalized count rates are plotted as a function of offset positions (θ). The three curves correspond to wavelength bins 125-140 nm (solid), 170-190 nm (dotted), and 225-240 nm (dashed). These plots represent the derived scattering function.

Figure 7. Normalized count rates are plotted as a function of offset positions (θ). The two sets of curves represent the wavelength bin 170-190 nm (upper set solid=in dispersion; dashed=cross dispersion) and the bin 95-115 nm (lower set dotted=in dispersion; dot/dash=cross dispersion).

Figure 8. Power law fit to the wings of the observed scattering function. The θ^{-3} fit corresponds most closely to predictions of the Airy disk, and not to a $\theta^{-2.19}$ fit predicted by surface microroughness. This result is consistent with the λ^{-1} fit for the wavelength dependence seen in Figure 9.

Figure 9. FOS Grating scatter. Upper Figure displays peak scattered light profile of FOS grating. Lower figure shows wings of profile. Measurements used a 50 micron exit slit to simulate the FOS digicon diode size. From Harms *et al*, "Astronomical Capabilities of the Faint Object Spectrograph on Space Telescope," IAU Commission 44, *The Space Telescope Observatory*, Aug. 1982.

Figure 10. Residual spectra for the offset position $\theta = 16''$, for both the in and cross dispersion directions. The λ^{-1} wavelength dependence is clearly seen and consistent with

a very high quality smooth HST mirror surface.

Figure 1

(a)

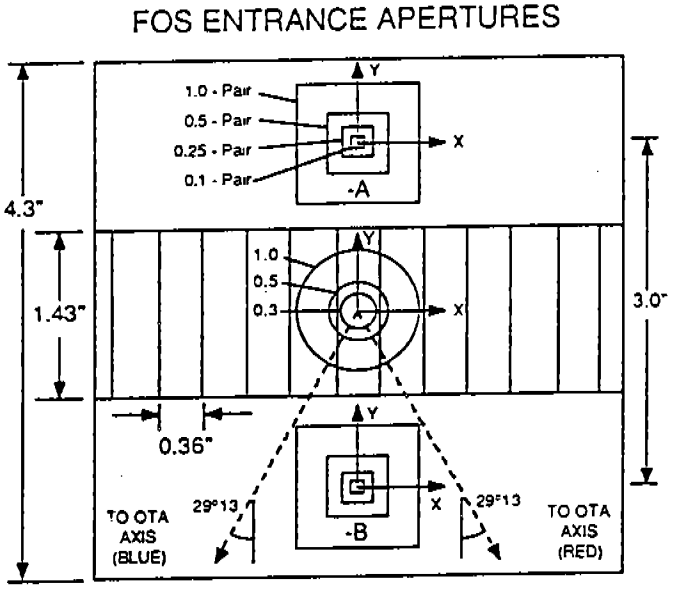
FOS ENTRANCE APERTURES
1.0 - Pair
0.5 - Pair
0.25 - Pair
0.1 - Pair
Y
X
-A
4.3"
1.43"
3.0"
1.0
0.5
0.3
0.36"
29°13
-B
TO OTA AXIS (BLUE)
TO OTA AXIS (RED)

(b)

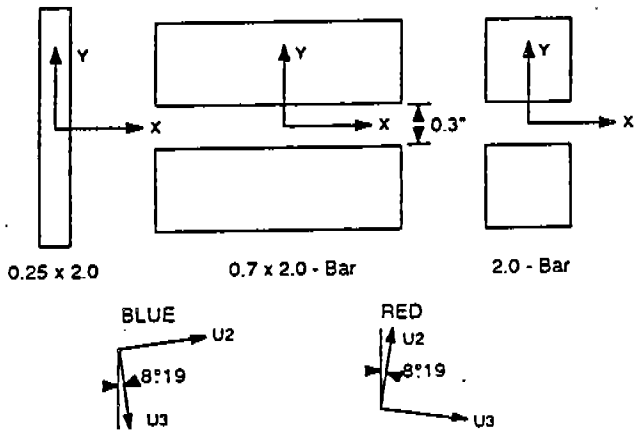
Y
X
0.3"
0.25 x 2.0
0.7 x 2.0 - Bar
2.0 - Bar
BLUE
U2
8°19
U3
RED

Figure2

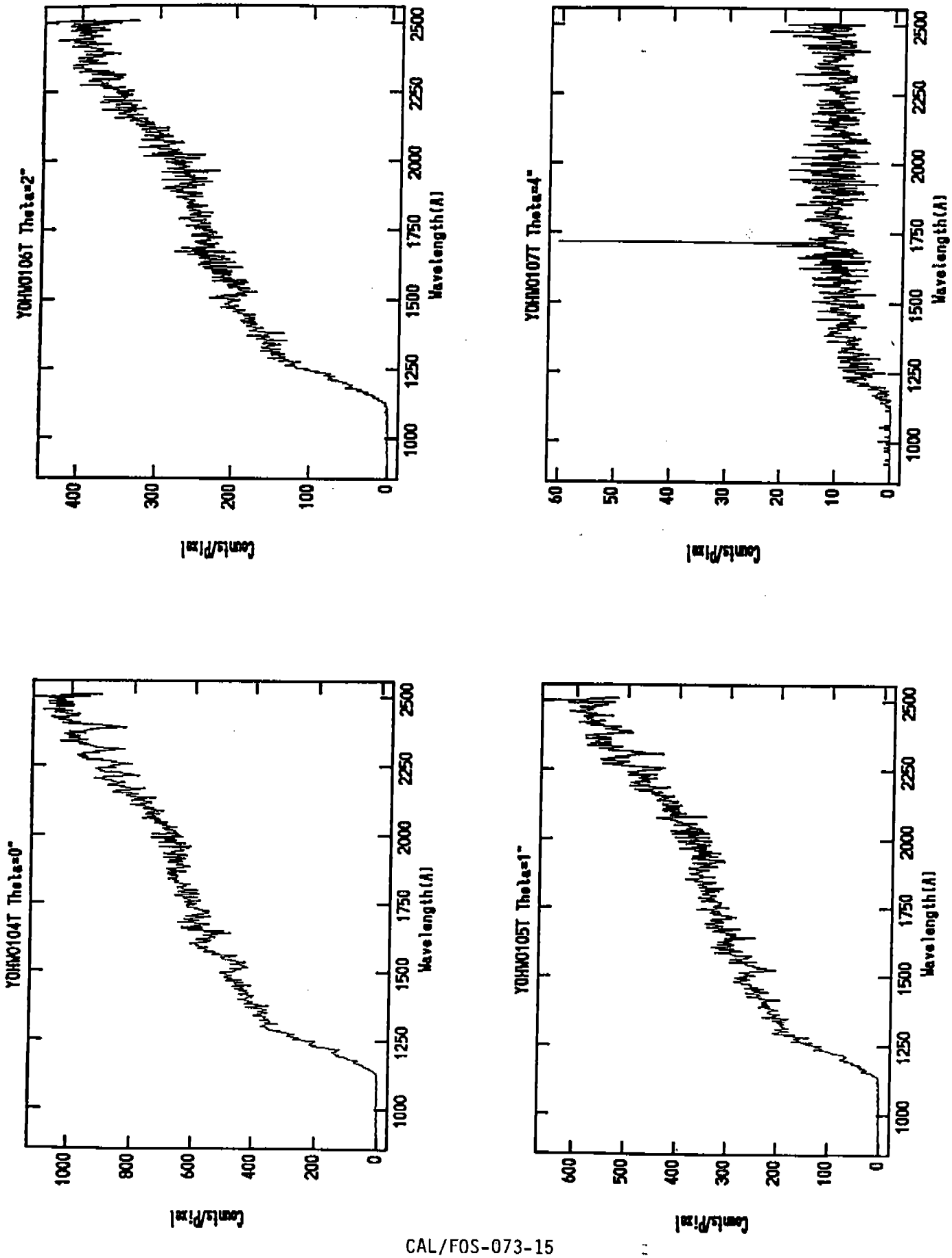
YOHM0106T Theta=2"
YOHM0107T Theta=4"
YOHM0104T Theta=0"
YOHM0105T Theta=1"
Counts/Pixel
Wavelength(A)

Figure 2 (cont.)

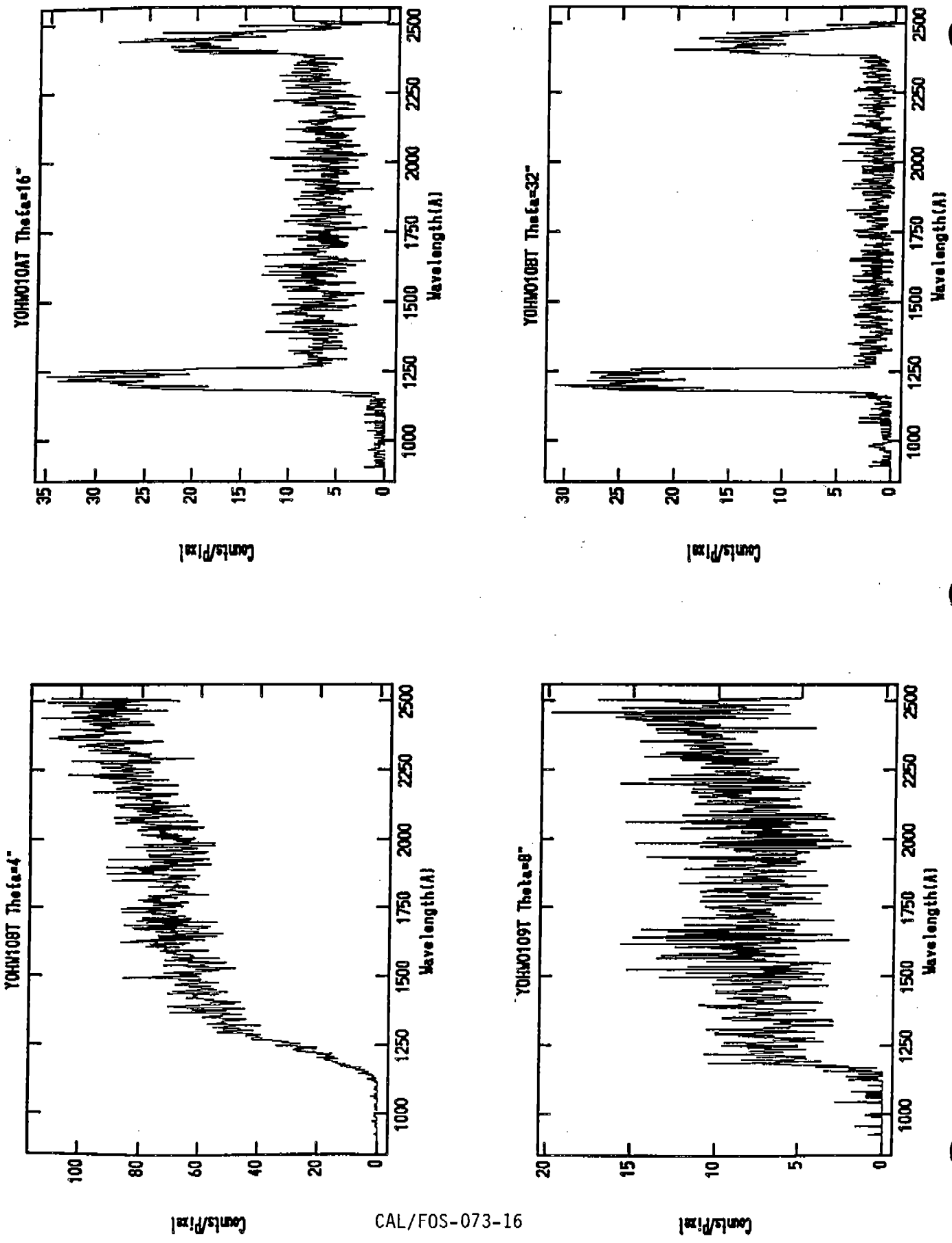

Figure 3

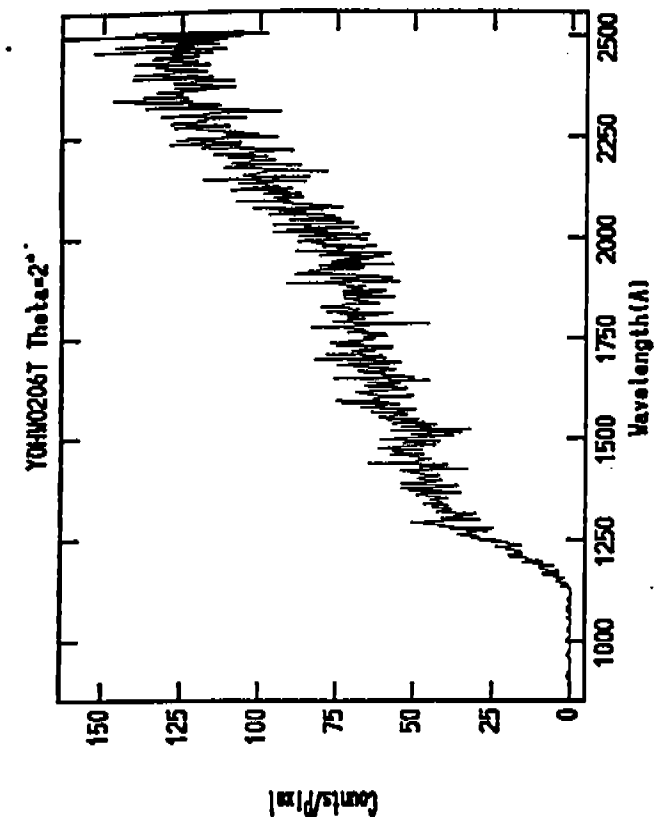
YOHM0206T Theta=2"
Counts/Pixel
Wavelength(A)

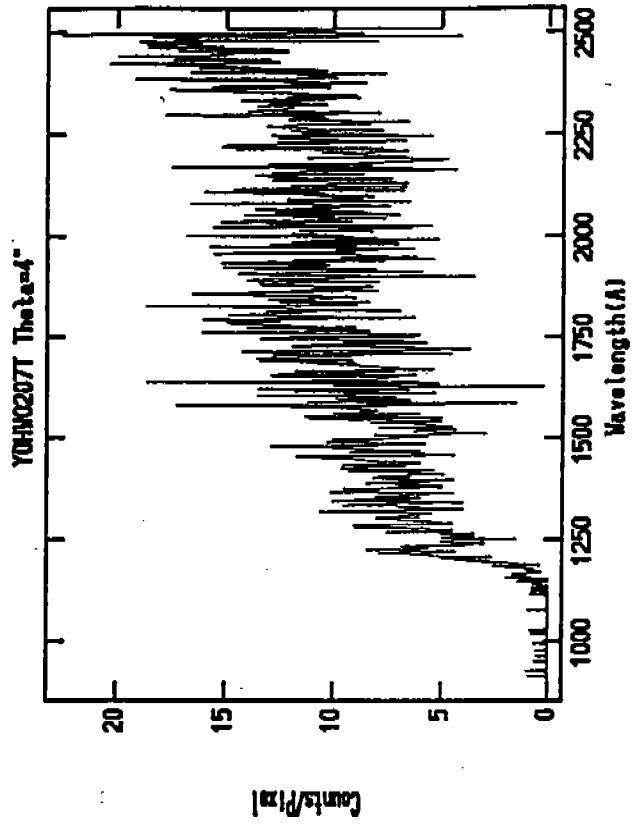
YOHM0207T Theta=4"
Counts/Pixel
Wavelength(A)

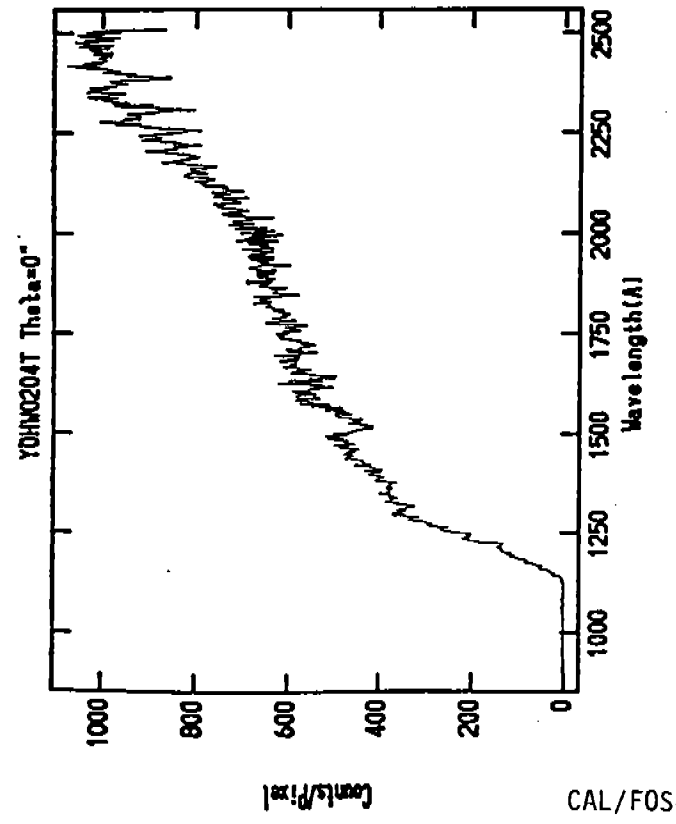
YOHM0204T Theta=0"
Counts/Pixel
Wavelength(A)

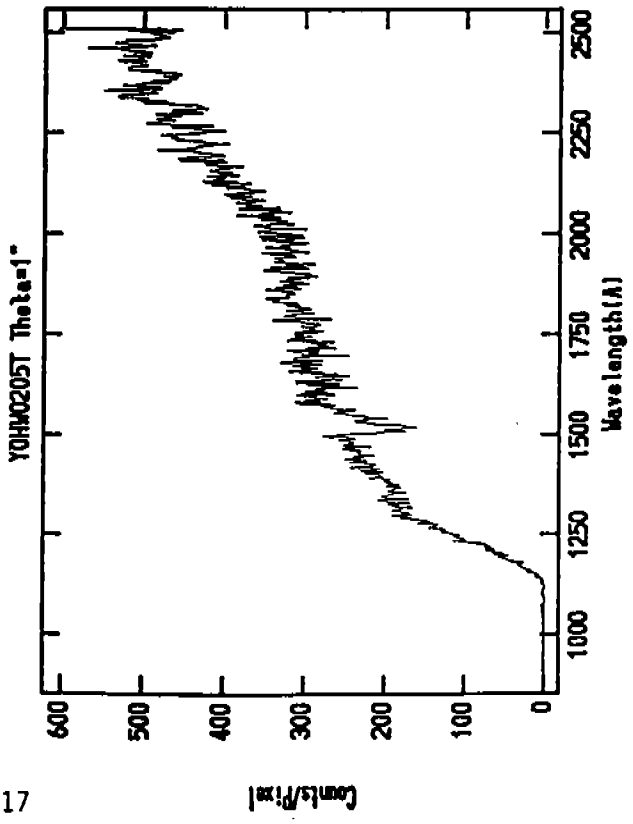
YOHM0205T Theta=1"
Counts/Pixel
Wavelength(A)

Figure 3 (cont.)

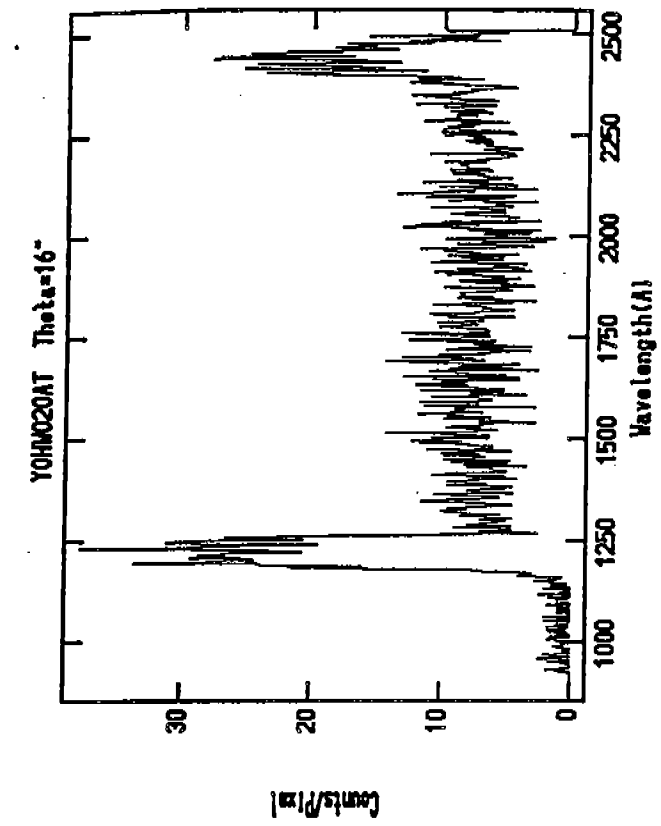

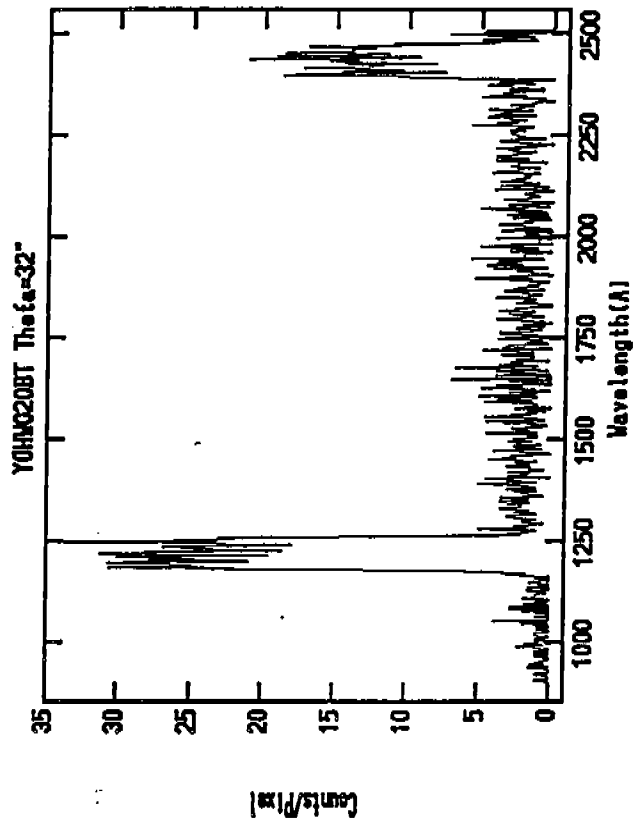

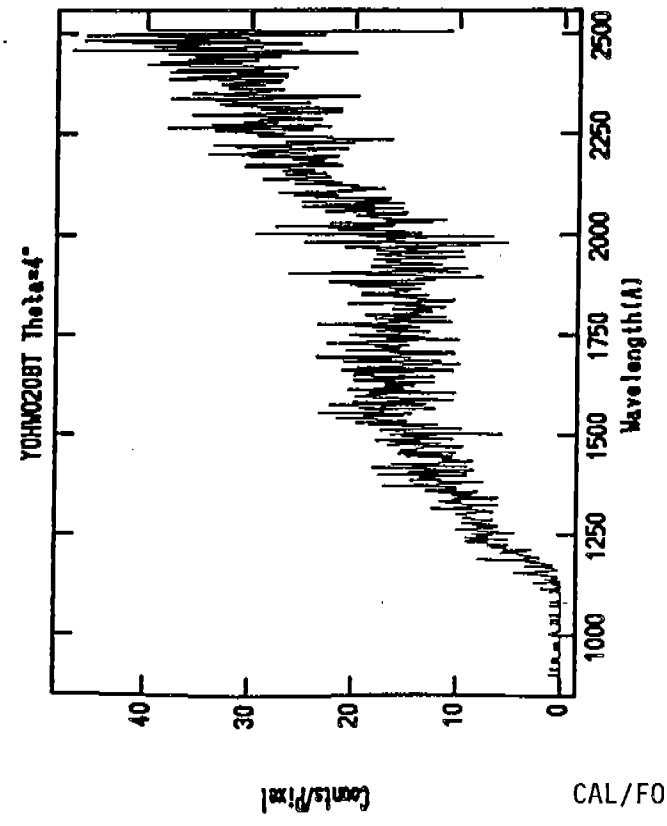

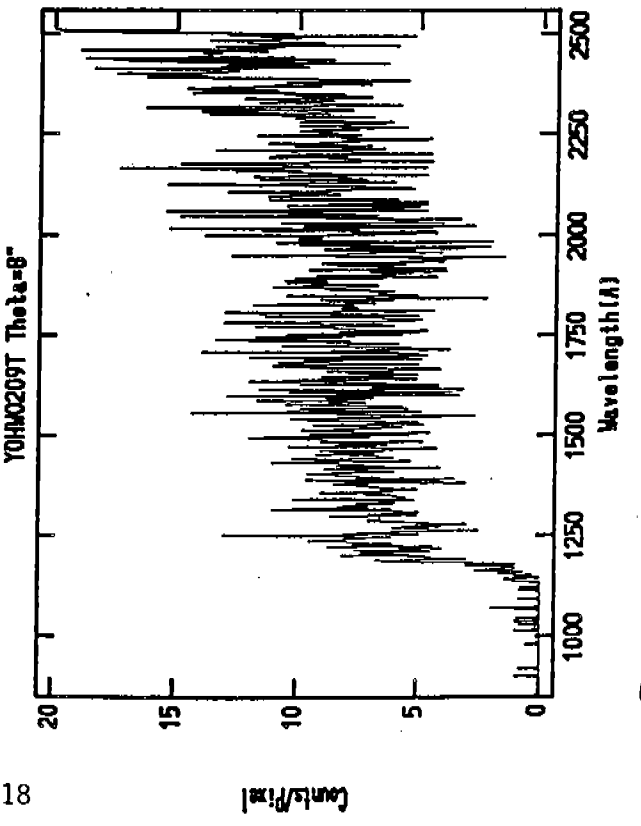

Figure 4

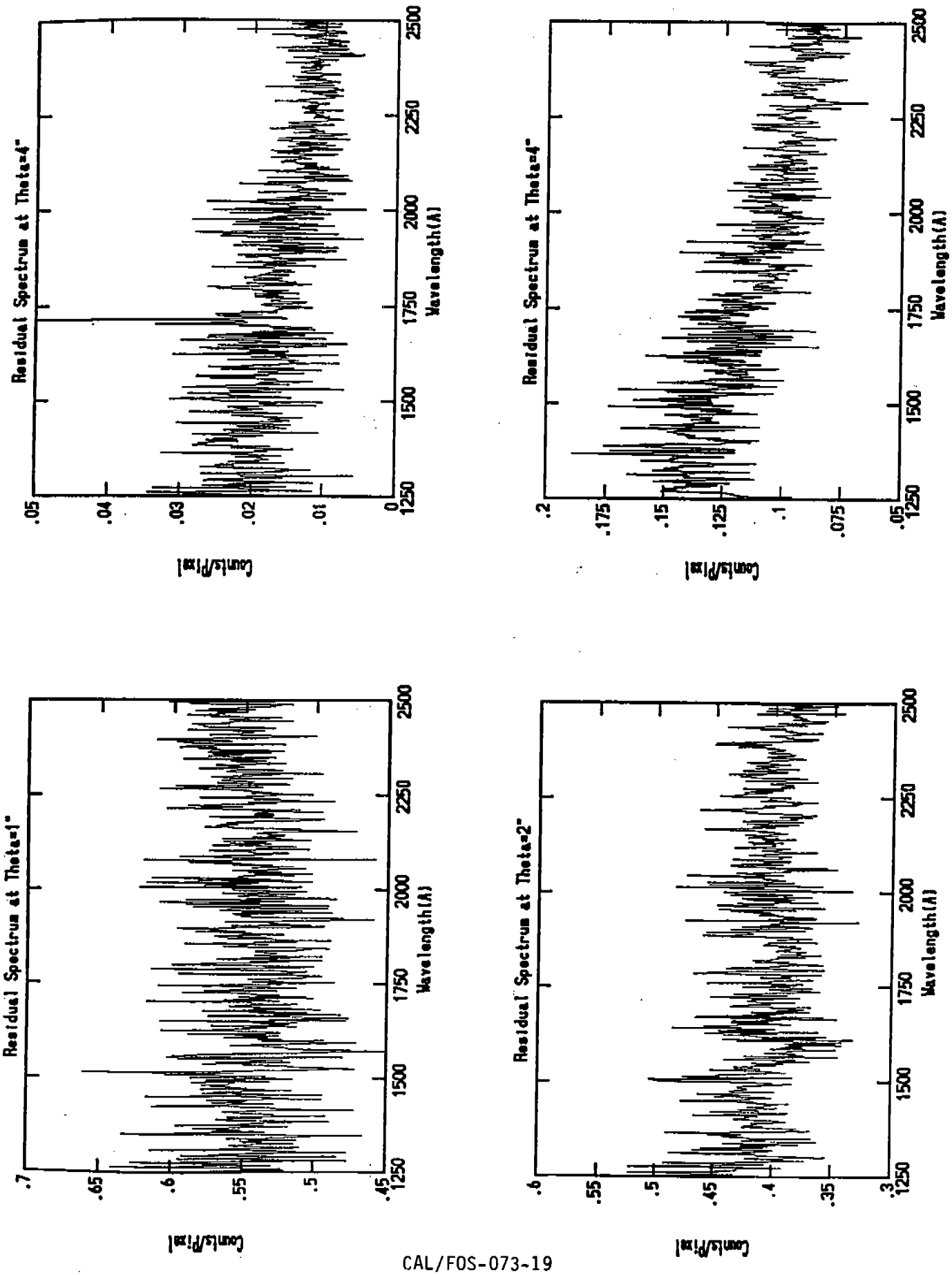
Residual Spectrum at Theta=4"
Counts/Pixel
Wavelength(A)
.05
.04
.03
.02
.01
0
1250
1500
1750
2000
2250
2500
Residual Spectrum at Theta=4"
Counts/Pixel
Wavelength(A)
.2
.175
.15
.125
.1
.075
.05
1250
1500
1750
2000
2250
2500
Residual Spectrum at Theta=1"
Counts/Pixel
Wavelength(A)
.7
.65
.6
.55
.5
.45
1250
1500
1750
2000
2250
2500
Residual Spectrum at Theta=2"
Counts/Pixel
Wavelength(A)
.6
.55
.5
.45
.4
.35
.3
1250
1500
1750
2000
2250
2500

Figure 4 (cont.)

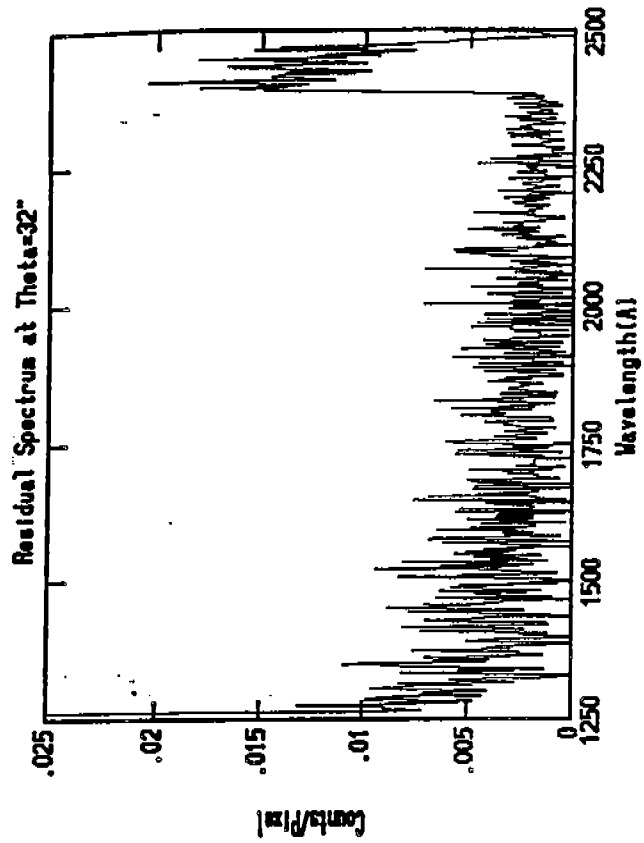

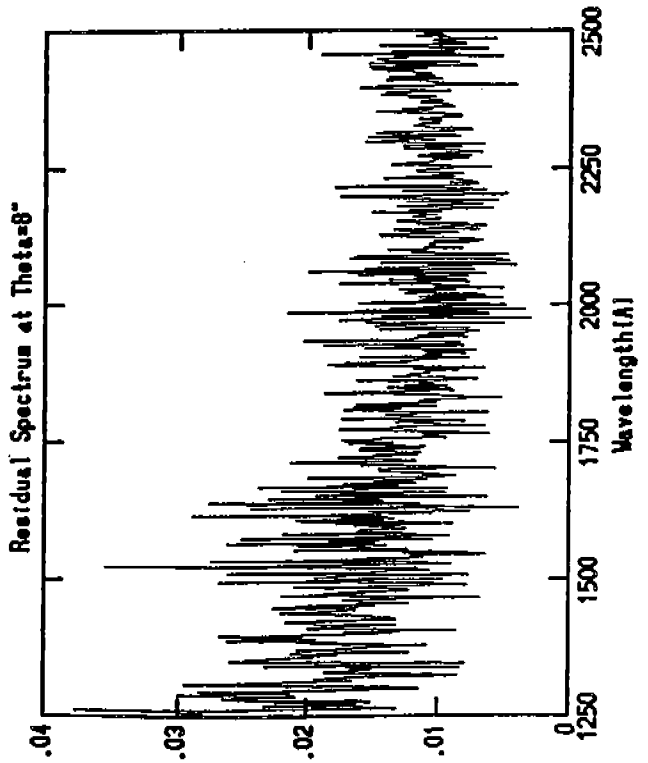

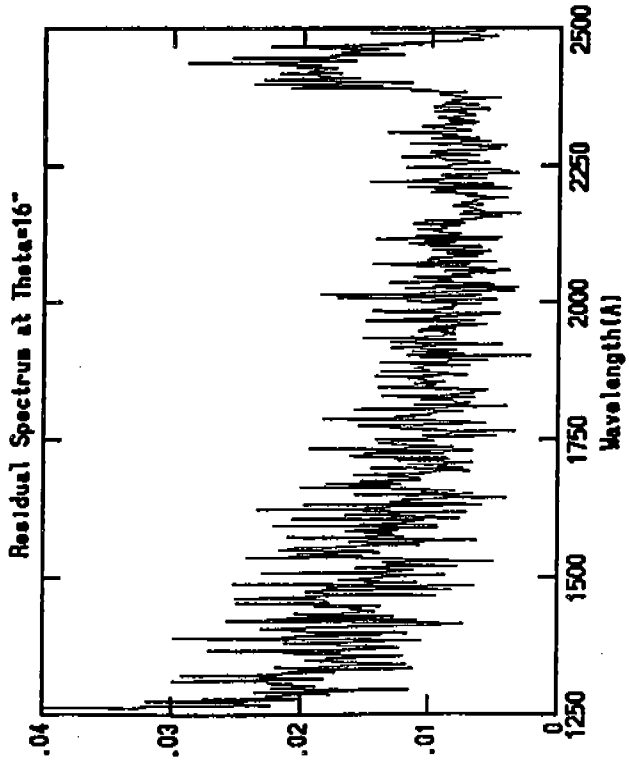

Figure 5

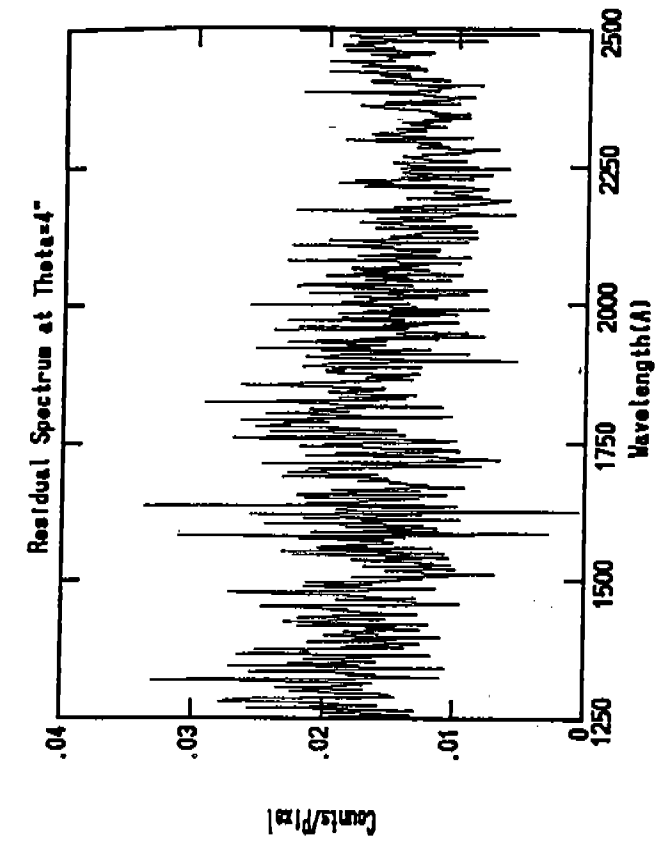
Residual Spectrum at Theta=4"
Counts/Pixel
Wavelength(A)
.04
.03
.02
.01
0
1250
1500
1750
2000
2250
2500

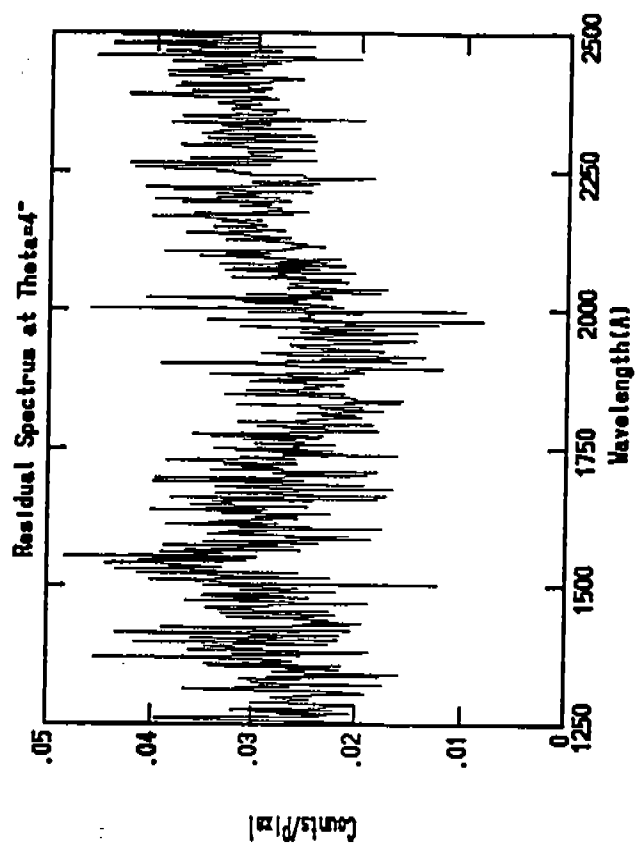
Residual Spectrum at Theta=4"
Counts/Pixel
Wavelength(A)
.05
.04
.03
.02
.01
0
1250
1500
1750
2000
2250
2500

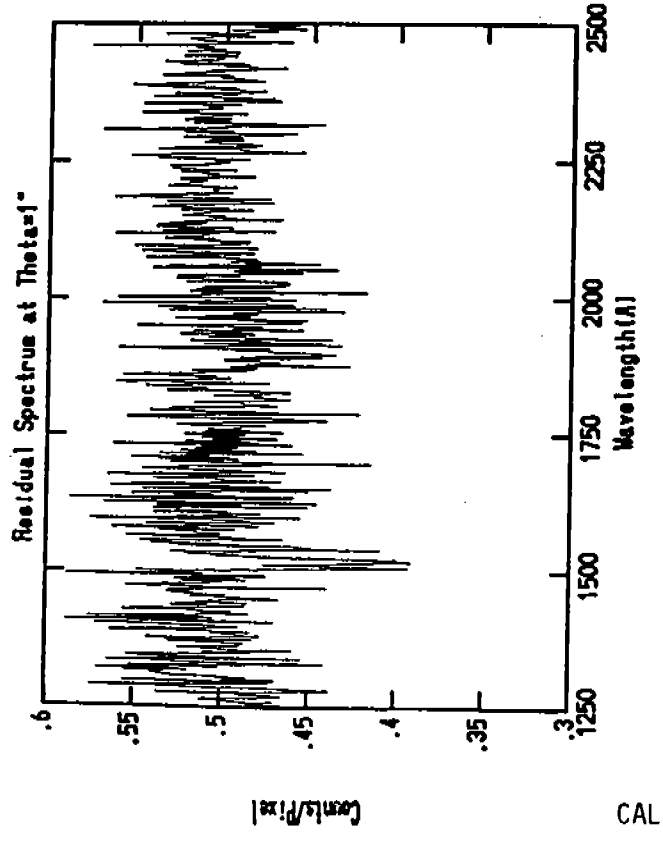
Residual Spectrum at Theta=1"
Counts/Pixel
Wavelength(A)
.6
.55
.5
.45
.4
.35
.3
1250
1500
1750
2000
2250
2500

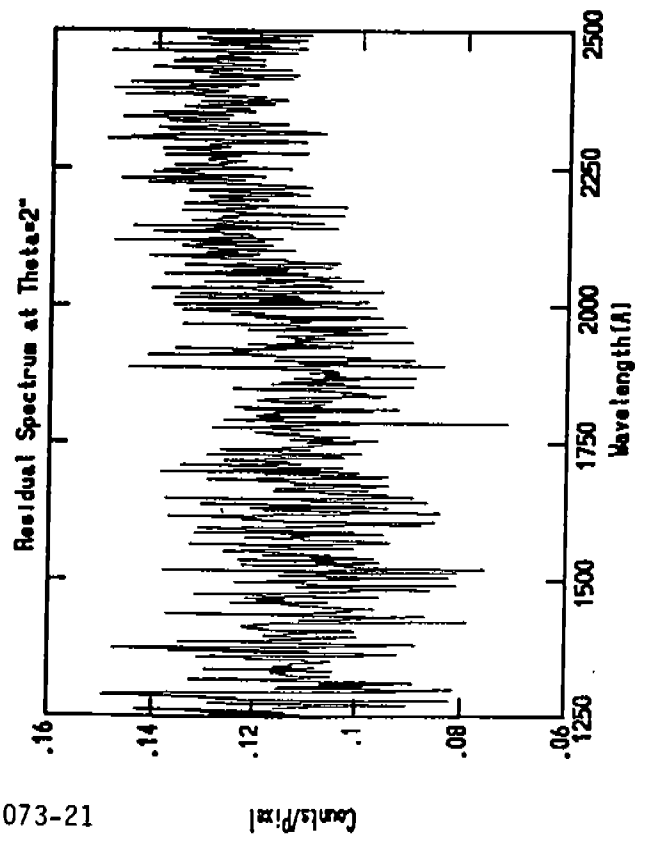
Residual Spectrum at Theta=2"
Counts/Pixel
Wavelength(A)
.16
.14
.12
.1
.08
.06
1250
1500
1750
2000
2250
2500

Figure 5 (cont.)

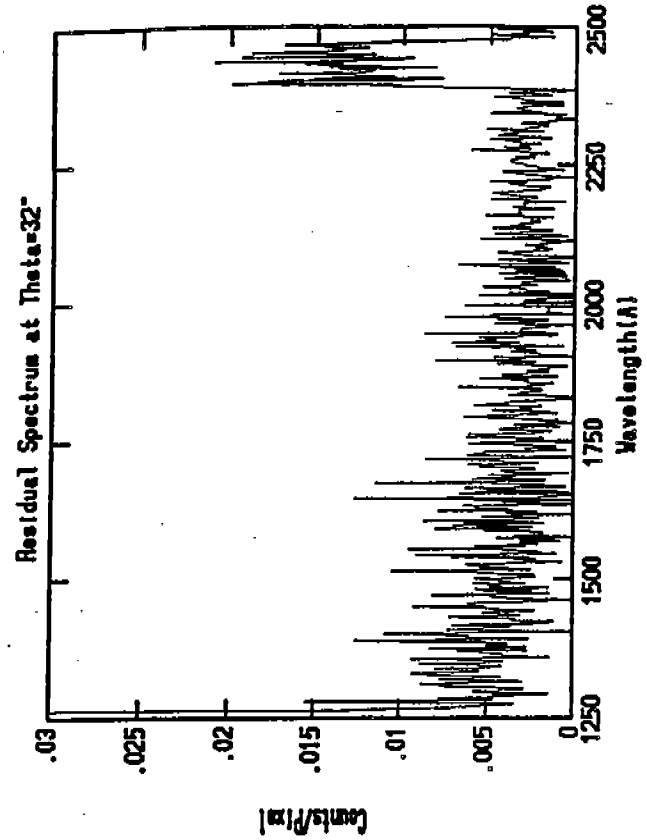

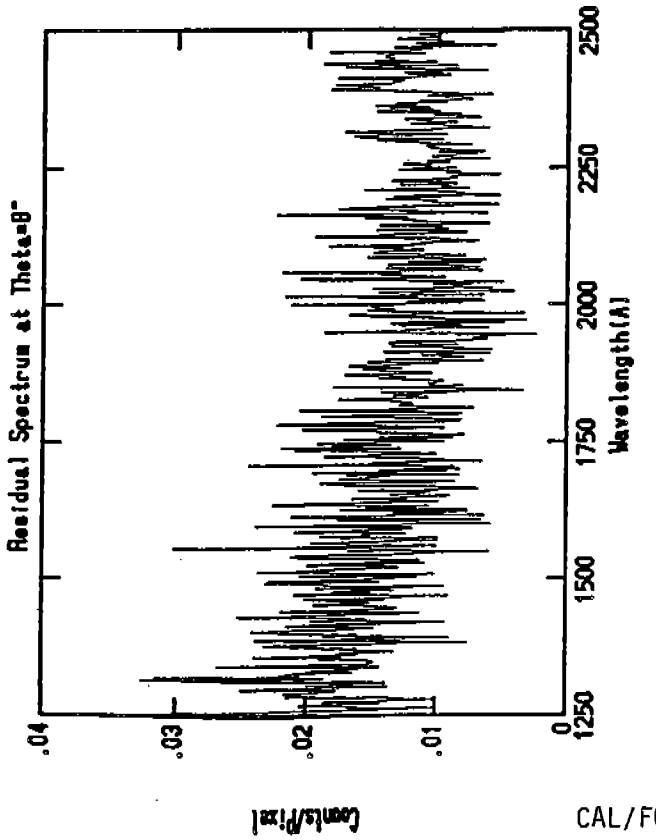

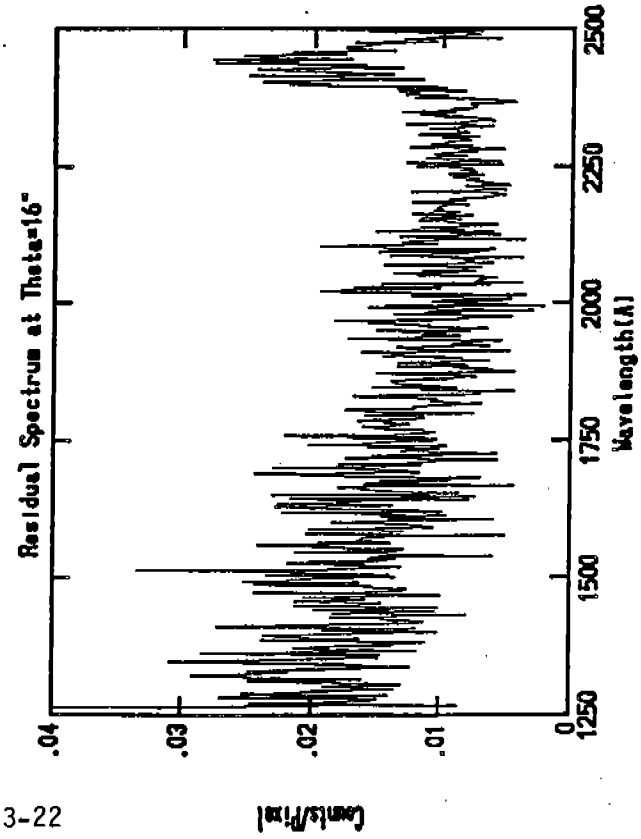

Figure 6

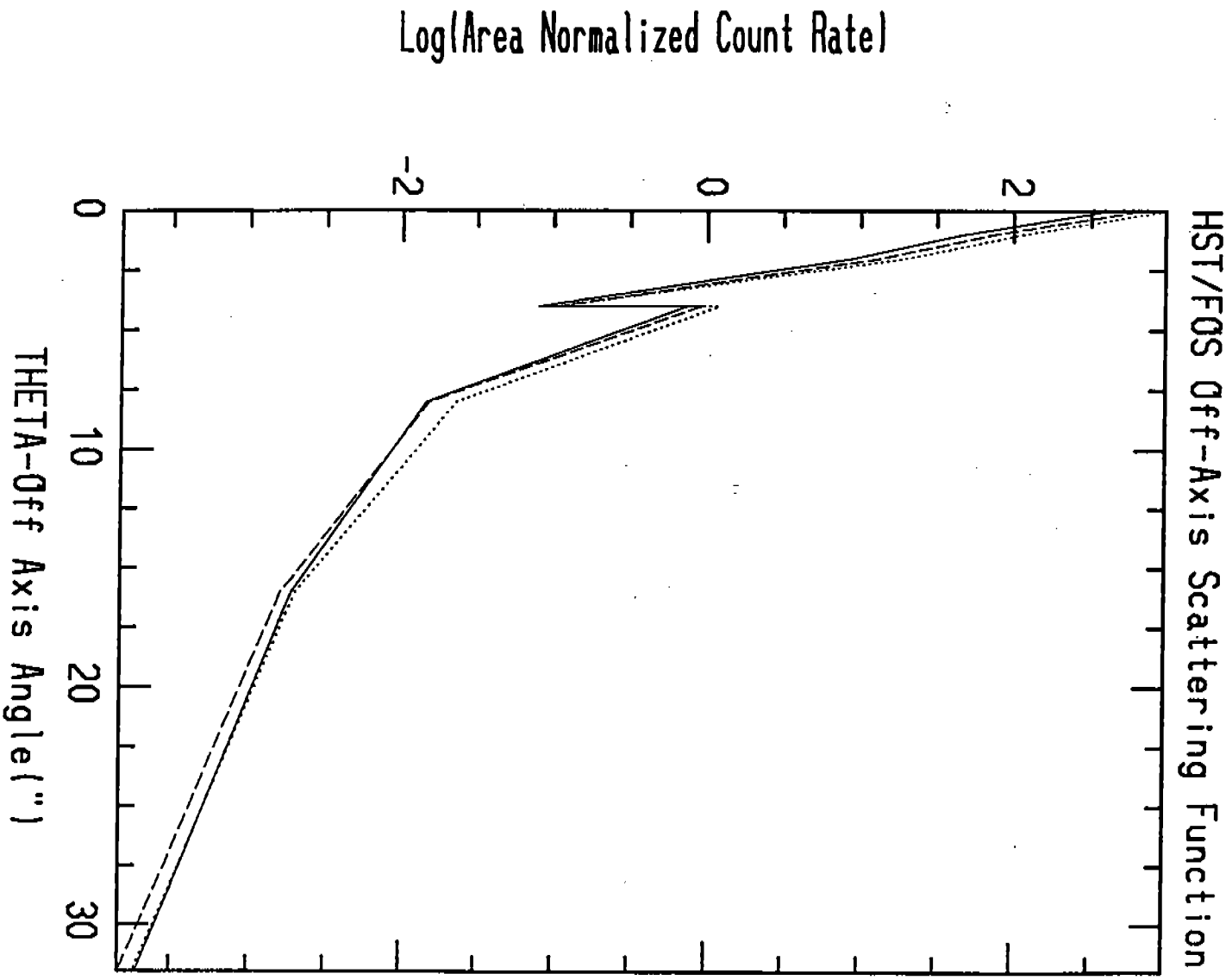

CAL/FOS-073-23

Figure 7

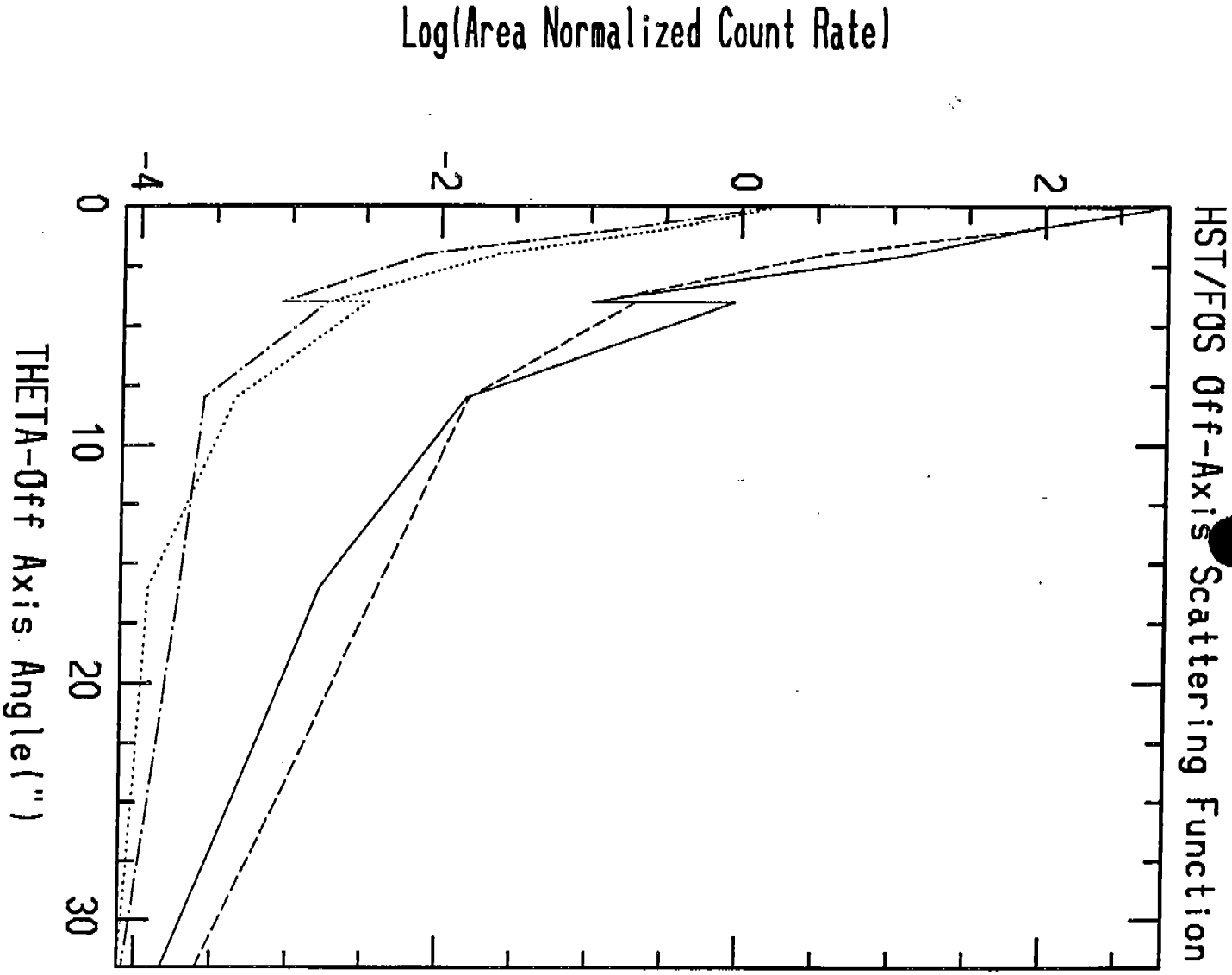

CAL/FOS-073-24

Figure 8

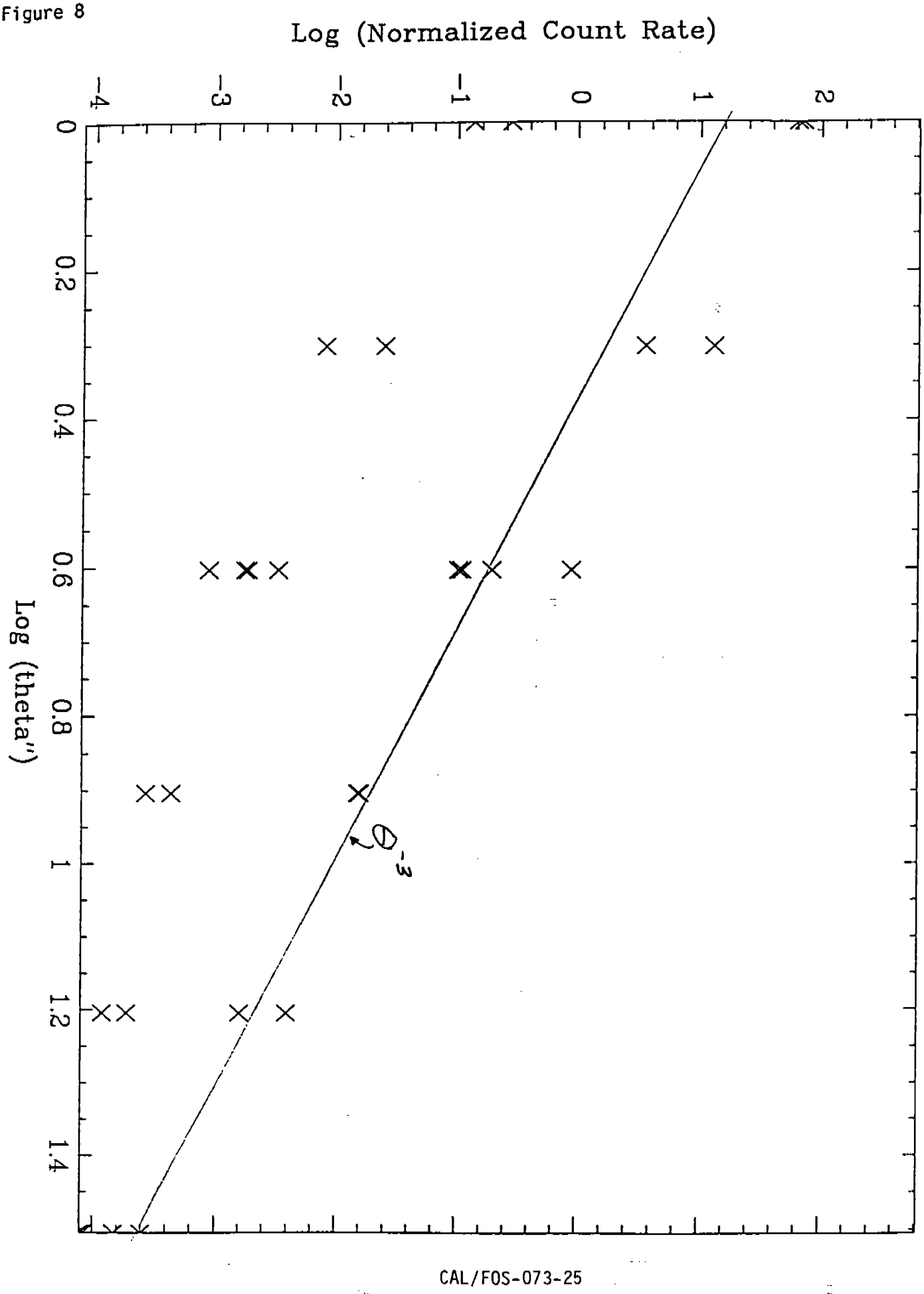

HST Scattered UV-Light measured with FOS

CAL/FOS-073-25

Figure 9

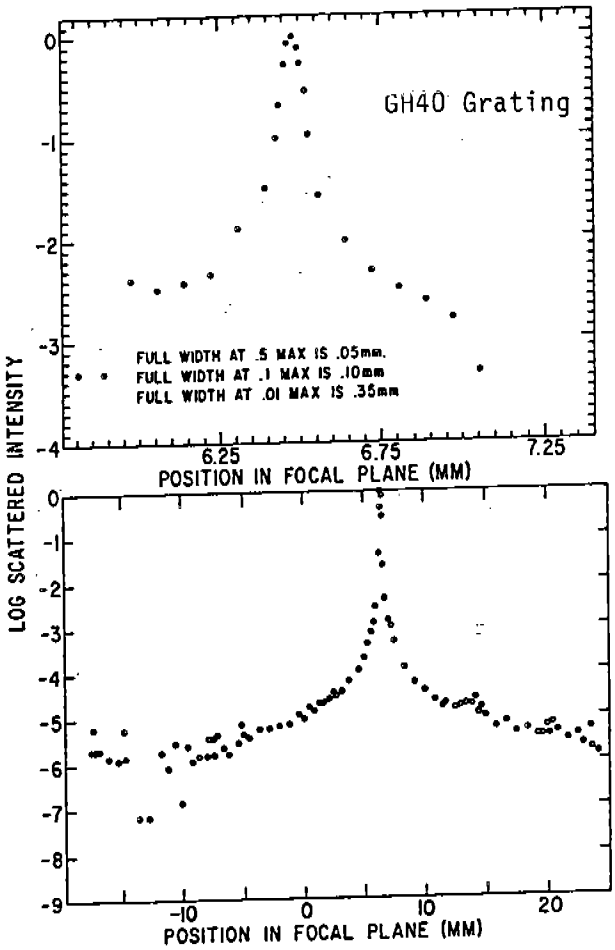

Upper figure displays peak scattered light profile of FOS flight grating; lower figure shows wings of profile. Measurement used 50 micron exit slit to match Digicon diode size.

Figure 10

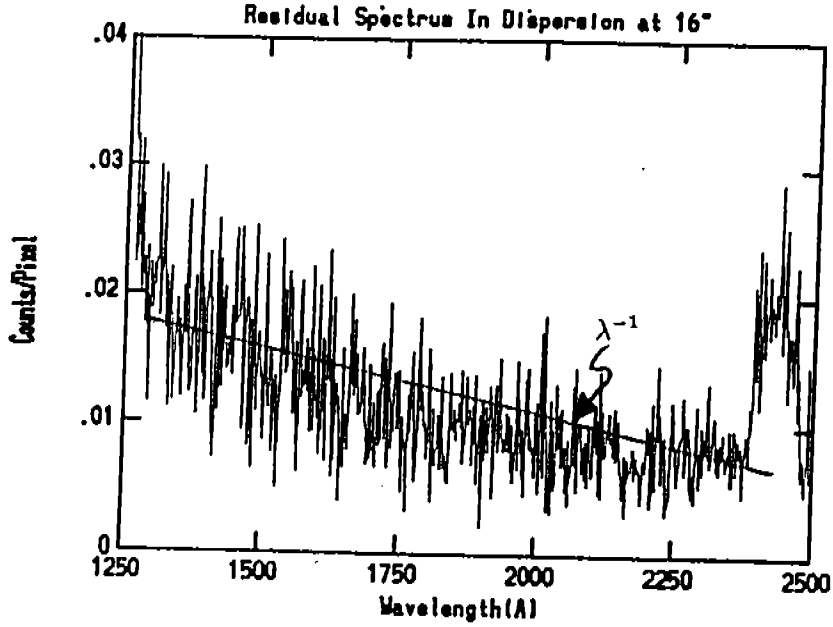
Residual Spectrum In Dispersion at 16"
Counts/Pixel
.04
.03
.02
.01
0
1250
1500
1750
2000
2250
2500
Wavelength(A)
λ^{-1}

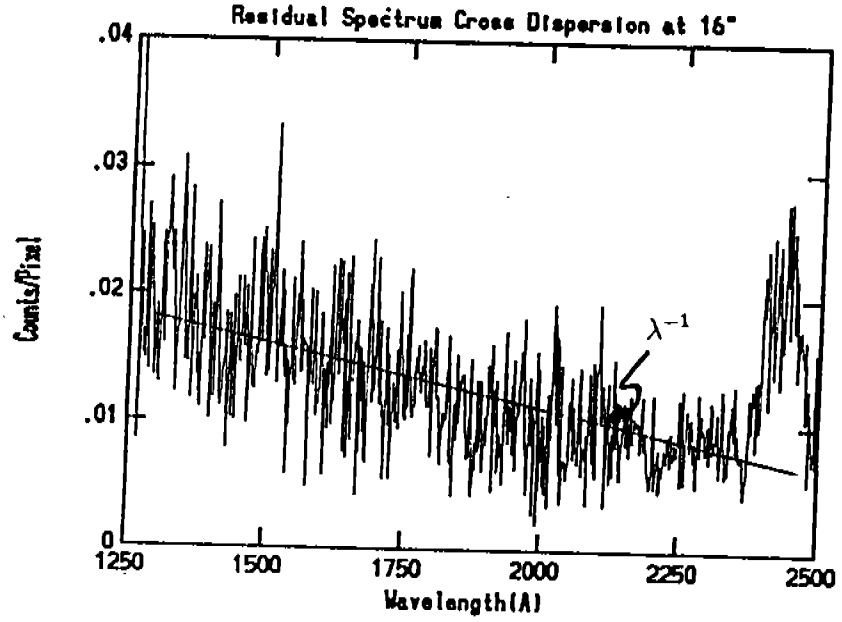
Residual Spectrum Cross Dispersion at 16"
Counts/Pixel
.04
.03
.02
.01
0
1250
1500
1750
2000
2250
2500
Wavelength(A)
λ^{-1}

Appendix A

Average of 125-140 nm in dispersion direction, normalized. Log of Average counts per second per square arc second.

angle	log (count rate)
0	2.612
1	1.650
2	0.930
4	-1.097
4	-0.135
8	-1.838
16	-2.728
32	-3.714

Average of 170-190 nm in dispersion direction, normalized. Log of Average counts per second per square arc second.

angle	log (count rate)
0	2.816
1.0	1.846
2.0	1.115
4.0	-0.988
4.0	-0.045
8.0	-1.818
16.0	-2.796
32.0	-3.826

Average of 225-240 nm in dispersion direction, normalized. Log of Average counts per second per square arc second.

angle	log (count rate)
0	2.993
1.0	2.040
2.0	1.287
4.0	-0.980
4.0	0.074
8.0	-1.637
16.0	-2.700
32.0	-3.732

Average of 170-190 nm cross dispersion direction, normalized. Log of Average counts per second per square arc second.

angle	log (count rate)
0	2.812
1	1.805
2	0.5539
4	-0.9594
4	-0.7081
8	-1.8031
16	-2.4057
32	-3.600

Average of lamda < 115 nm, in dispersion direction, normalized. Log of Average counts per second per square arc second.

angle	log (count rate)
0.0	0.2702
1.0	-0.5600
2.0	-1.6108
4.0	-2.7380
4.0	-2.4841
8.0	-3.3655
16.0	-3.9281
32.0	-4.1057

Average of lamda < 115 nm, cross dispersion direction, normalized. Log of Average counts per second per square arc second.

angle	log (count rate)
0.0	0.2188
1.0	-0.8687
2.0	-2.0980
4.0	-3.0629
4.001	-2.7612
8.0	-3.5735
16.0	-3.7258
32.0	-4.0783